







RESEARCH ARTICLE | SEPTEMBER 22 2023

Radio frequency electrical resistance measurement under destructive pulsed magnetic fields

T. Shitaokoshi  ; S. Kawachi  ; T. Nomura  ; F. F. Balakirev  ; Y. Kohama  



Rev. Sci. Instrum. 94, 094706 (2023)

<https://doi.org/10.1063/5.0165680>



CrossMark



APL Machine Learning
Latest Articles Online!
Read Now



Radio frequency electrical resistance measurement under destructive pulsed magnetic fields

Cite as: Rev. Sci. Instrum. 94, 094706 (2023); doi: 10.1063/5.0165680

Submitted: 29 June 2023 • Accepted: 30 August 2023 •

Published Online: 22 September 2023



View Online



Export Citation



CrossMark

T. Shitaokoshi,¹  S. Kawachi,^{2,3}  T. Nomura,^{1,4}  F. F. Balakirev,⁵  and Y. Kohama^{1,a)} 

AFFILIATIONS

¹Institute for Solid State Physics, The University of Tokyo, Kashiwa, Chiba 277-8581, Japan

²Materials Research Center for Element Strategy, Tokyo Institute of Technology, Yokohama, Kanagawa 226-8503, Japan

³Graduate School of Science, University of Hyogo, Ako, Hyogo 678-1297, Japan

⁴School of Engineering, Tokyo Denki University, Adachi, Tokyo 120-8551, Japan

⁵National High Magnetic Field Laboratory, Los Alamos National Laboratory, Los Alamos, New Mexico 87545, USA

^{a)}Author to whom correspondence should be addressed: ykohama@issp.u-tokyo.ac.jp

ABSTRACT

We developed a resistance measurement using radio frequency reflection to investigate the electrical transport characteristics under destructive pulsed magnetic fields above 100 T. A sample stage consisting of a homemade flexible printed circuit reduced the noise caused by the induced voltage from the pulsed magnetic fields, improving the accuracy of the measurements of the reflected waves. From the obtained reflectance data, the absolute value of the magnetoresistance was successfully determined by analyzing the phase with admittance charts. These developments enable more accurate and comprehensive measurements of electrical resistance in pulsed magnetic fields.

Published under an exclusive license by AIP Publishing. <https://doi.org/10.1063/5.0165680>

I. INTRODUCTION

In the study of metals and their transport properties, the measurement of electrical resistivity in high magnetic fields plays a crucial role. Conventional approaches for measuring magnetoresistance have relied on standard alternating current (AC) techniques, typically conducted at magnetic fields below 100 T, generated by non-destructive pulsed magnets. However, performing magnetoresistance measurements in higher magnetic fields exceeding 100 T has been a significant challenge, requiring the use of destructive pulse magnets such as a single-turn coil (STC). The STC, while capable of generating high magnetic fields up to ~ 200 T,¹ has an extremely short field duration of several microseconds, accompanied by significant electrical noise due to its destructive nature, which is unsuitable for conventional resistance measurements.

In previous attempts to measure the electrical resistivity of metallic samples in strong magnetic fields generated by the STC, several approaches were applied, including the four-terminal,²⁻⁴ millimeter-wave transmission,⁵ radio frequency (RF)

transmission,⁶⁻⁸ and self-resonant RF reflection measurements.⁹ However, most of these works faced challenges due to the rapid sweep rate of the STC ($\sim 10^8$ T/s), which induces a huge voltage ($\sim 10^2$ V) in the circuit in proportion to its cross-sectional area perpendicular to the magnetic field. This significant voltage prevents accurate measurements in these experiments.

In recent years, an alternative approach has been developed,¹⁰ which employs a flexible printed circuit (FPC) that is laid parallel to the magnetic field and has an extremely small cross-sectional area perpendicular to the field. This configuration minimizes the induced voltage to an optimal level, allowing it to be used as a voltage source for resistivity measurements. However, in this technique, the induced voltage becomes zero near the peak of the pulsed magnetic field, which losses sensitivity around the maximum field region.

Among the previous approaches, the RF impedance measurement,¹¹⁻¹⁵ which utilizes the relationship between the reflectance of RF waves and electrical impedance, enables one to perform measurements at the peak of the magnetic field. In the conventional RF impedance measurements, a directional coupler

was used to separate RF waves.^{11–13} However, the weak coupling between the input and the coupled ports of the directional coupler resulted in insufficient separation of the reflected waves. This led to weak signals and a low signal-to-noise (S/N) ratio, compromising the accuracy and reliability of the measurements. In addition, the transmission line used in the conventional setup consisted of a twisted pair of copper wires, which was not fully impedance-matched and prevented RF propagation. Moreover, the small loops formed in the twisted pair resulted in excess induced voltage, introducing noise into the measurements. Furthermore, the imaginary part of the reflection coefficient was not appropriately analyzed, resulting in inaccurate resistance values. Therefore, there was a need for an improvement in the measurement setup and the analytical method to enhance the accuracy of the resistance measurements and to fully utilize the information of the reflection coefficient.

In this paper, we will introduce a setup for the RF impedance measurement utilizing a circulator instead of a directional coupler for the RF wave separation, and an FPC instead of a twisted pair for noise reduction. Furthermore, we present a novel analytical method for obtaining magnetoresistance data, where the reflection coefficient is treated as a complex number, using an admittance chart. In the following sections, we will explain the measurement setup, theoretical foundations, and practical data analysis using the result obtained with a non-destructive pulse magnet. We will also present the results obtained with an STC. Comparative studies with conventional methods will be included to highlight the advantages and limitations of our approach.

II. METHOD

A. Experiment

Figure 1(a) shows the block diagram of an RF impedance-measurement system, which consists of an RF generator, oscillo-

scope, splitter, circulator, terminator, filter, attenuator, pickup coil, and FPC. A RF sine wave of 125 or 250 MHz was generated by the combination of a bandpass filter with a Crystek CPRO33 or a CRBSCS-01 clock oscillator, respectively. The RF sine wave between 130 and 140 MHz was generated by the Stanford Research Systems SG382 signal generator. The signals were split in two by the Mini-Circuits ZFSC-2-1-S+ splitter. Half of the signals were measured as a reference wave by the Teledyne LeCroy HDO4104A oscilloscope, while the other half were transmitted to the conducting sample on the FPC via the circulator. The Admotech ADC012CSLH(50)-B circulator was used for the measurements between 125 and 140 MHz, and ADC028CSLH(80) for the measurements at 250 MHz. These results were compared with those at 125 MHz, where the circulator was replaced by a directional coupler (Mini-Circuits ZFDC-10-1+).

The reflected waves from the sample were separated by the circulator or the directional coupler and recorded by the oscilloscope after passing through a bandpass filter. Our circulator has three ports; when a signal is incident on one port, the circulator transmits it to the next port. On the other hand, our directional coupler is a device that extracts a portion of the signal propagating in a particular direction along the transmission line. To prevent unwanted RF reflections at the input of the oscilloscope and to protect the oscilloscope from the spike noise induced by the field generation, external 50 Ω terminators were connected prior to the oscilloscope, and input impedances of the oscilloscope were set to 1 MΩ. The reflected waves and the reference waves were numerically treated with the lock-in technique, and the reflectance $\Gamma = A_2/A_1$ and the phase shift $\theta = \theta_2 - \theta_1$ were obtained, where A_1 and A_2 are the amplitudes of the reference and reflected waves and θ_1 and θ_2 are the phases of the reference and reflected waves, respectively [See Fig. 1(b)]. However, it is noteworthy that the obtained Γ and θ are not the actual reflectance and phase shift due to the reflection at the sample, because the RF wave propagates in the cable before being captured in the oscilloscope and makes an attenuation and

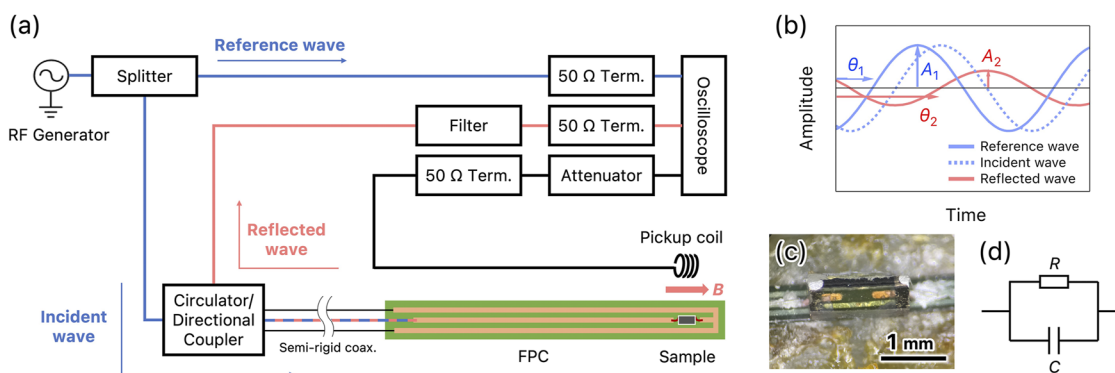


FIG. 1. (a) Block diagram of the RF measurements. Signal from an RF generator is split in two, and one-half of the signal is captured as a reference wave, and the other half is sent via a circulator or directional coupler to a conductive sample mounted on an FPC. The reflected signal from the sample is separated at the circulator or directional coupler and captured after passing through the bandpass filter. 50 Ω terminators are attached to each input. (b) Schematic diagram of the amplitudes and phases of the incident (blue dotted line), reflected (red solid line), and reference waves (blue solid line). A_1 and A_2 show the amplitudes of the reference and reflected waves, respectively. θ_1 and θ_2 show the phases of the reference and reflected waves, respectively. The amplitude and the phase of the RF wave change due to the reflection at the sample. The phase of the reference wave is shifted from that of the incident wave owing to the cable length. (c) Photo of a conductive sample mounted on the FPC. A YBCO thin film (black) on MgO substrate (transparent) was attached with gold wires and silver paste. (d) An equivalent circuit around the sample. R and C represent the resistance of the sample and the parasitic capacitance associated with the wires and other components, respectively.

extra phase shift. The wavelength of the RF wave used here is around 1–2 m, and the total length of the transmission line is ~ 10 m, which results in an extra phase shift of $20\text{--}10\pi$. To eliminate this background, a constant value must be subtracted from the raw phase data.

Measurements at low temperatures and under pulsed magnetic fields were conducted in a plastic or metal cryostat using a measurement probe consisting of a 10 cm-long FPC, a 90 cm-long semi-rigid coaxial cable, and a fiber-reinforced plastic rod. The FPC fabricated by Taiyo Industrial consisted of a three-line microstrip array^{16,17} connected to the semi-rigid coaxial cable, with solder at one of the ends. The three lines were connected at the opposite end, and the central line had a gap to accommodate a metallic sample [Fig. 1(c)]. The two outer lines were grounded, functioning as electromagnetic shields. Each line had a width of $100\ \mu\text{m}$, and they were spaced $50\ \mu\text{m}$ apart from each other. The FPC and semi-rigid coaxial cable were glued to the fiber-reinforced plastic rod. The characteristic impedance of the FPC (Z_0) is designed to be around $50\ \Omega$. The magnetic fields were generated by a non-destructive pulse magnet and an STC. The time durations of these field pulses were 38 ms and $7\ \mu\text{s}$, respectively. The field strength was calculated by integrating the voltage induced in the pickup coil.

One of the test samples used for this work was kish graphite, which was micro-processed using focused ion beam (FIB) technology. The sample dimensions after processing were $\sim 100 \times 25 \times 10\ \mu\text{m}^3$. The graphite sample was mounted on the FPC using gold wires and silver epoxy. Measurements in the non-destructive pulsed magnetic fields were conducted at 4.2 K using liquid helium by applying the field along the c axis of graphite. The other test sample was a $\text{YBa}_2\text{Cu}_3\text{O}_7$ (YBCO) thin film grown on MgO substrate, which was purchased from CERACO Ltd. The YBCO film has a slight excess of copper and shows the superconducting transition at ~ 86 K. The YBCO film had a thickness of $500\ \text{nm}$ and was cut into the dimensions of $1500 \times 100\ \mu\text{m}^2$. Two different film samples were prepared from the same batch of the YBCO film and used for the experiments at the STC (sample 1) and non-destructive magnet (sample 2). The measurements were conducted between 77.4 and 87.5 K using liquid nitrogen, by applying the magnetic field within the ab plane. In addition to the above test samples, small chip resistors ranging from 30 to $100\ \Omega$ were also mounted on the FPC, and the performance of the probe was checked under zero magnetic field at 77.4 K.

To check the validity of our technique, standard two-terminal resistance measurements were also performed using the same probe at low frequency (50 kHz) with a non-destructive pulsed magnet. The circulator or the directional coupler was removed, and a shunt resistor was connected in series with the sample. The voltage between each end of the sample (V) and the shunt resistor (V_{shunt}) was measured. The two-terminal resistance of the sample was calculated by $R = R_{\text{shunt}}V/V_{\text{shunt}}$, where R and R_{shunt} are the resistance of the sample and shunt resistor, respectively.

B. Analysis

The actual reflectance Γ_S at the sample, which is the ratio between the amplitudes of the incident and reflected waves, and the actual phase shift θ_S caused by the reflection at the sample can be transformed into polar coordinates to define the complex reflection coefficient

$$\rho = \Gamma_S e^{i\theta_S} = u + iv, \quad (1)$$

where u and v are the real and imaginary parts of the complex coefficient, respectively. In this analysis, the sample connected to the FPC with wires was treated as a parallel circuit consisting of a real resistance R and a parasitic capacitance C [See Fig. 1(d)],¹⁸ and the admittance of this parallel RC circuit was considered. The relationship between the normalized admittance $y = YZ_0$ (Y : admittance and Z_0 : characteristic impedance) and the complex reflection coefficient ρ is given by¹⁹

$$y = \frac{1 - \rho}{1 + \rho}. \quad (2)$$

Complex numbers $y = g + ib$ and $\rho = u + iv$ are substituted into this equation, where g and b are the normalized conductance and susceptance, respectively. By comparing the real and imaginary parts of Eq. (2), one can obtain

$$g = \frac{1 - u^2 - v^2}{(1 + u)^2 + v^2}, \quad (3)$$

$$b = -\frac{2v}{(1 + u)^2 + v^2}. \quad (4)$$

The relationship obtained from Eqs. (3) and (4) represent circles in the uv -plane, the so-called admittance chart. The admittance chart is a graphical calculator used for electronic circuit design in the field of RF engineering, forming a complementary pair with the Smith chart.^{19–22} When ρ is plotted on the uv -plane along with an admittance chart, it tells the conductance and susceptance of the sample. This means that, by measuring the variation of ρ with the magnetic field and plotting it with an admittance chart, one can convert it into the field dependence of the conductance and susceptance.

III. RESULTS

A. Measurements with a non-destructive magnet

Figure 2(a) shows the magnetoresistance of FIB-processed graphite, measured by the standard two-terminal technique at a frequency of 50 kHz. The magnetic field was generated by the non-destructive pulsed magnet, and the sample was immersed into liquid helium at 4.2 K. Graphite exhibits a large magnetoresistance in relatively weak magnetic fields, which is appropriate for testing the validity of the analysis proposed in the previous section.

Figure 2(b) displays the RF reflectance Γ measured at 125 and 250 MHz, using the circulator or directional coupler. In all setups, a dip was observed in Γ , where the magnetoresistance of the sample reaches the characteristic impedance Z_0 ($\sim 50\ \Omega$), and the reflection is minimized due to the impedance matching (gray hatched area). The magnetic field where the dip appears depends on the frequency or the measurement setup because of the variation of Z_0 . The use of the circulator instead of the directional coupler results in lower losses and larger reflection signals.

Figure 2(c) illustrates the field dependence of the phase shift θ_S obtained from RF measurements at 125 and 250 MHz. A constant background is subtracted from the raw phase data. The phase shift is caused by the reflection from the sample, and it depends on its admittance. Around zero magnetic field, where the sample

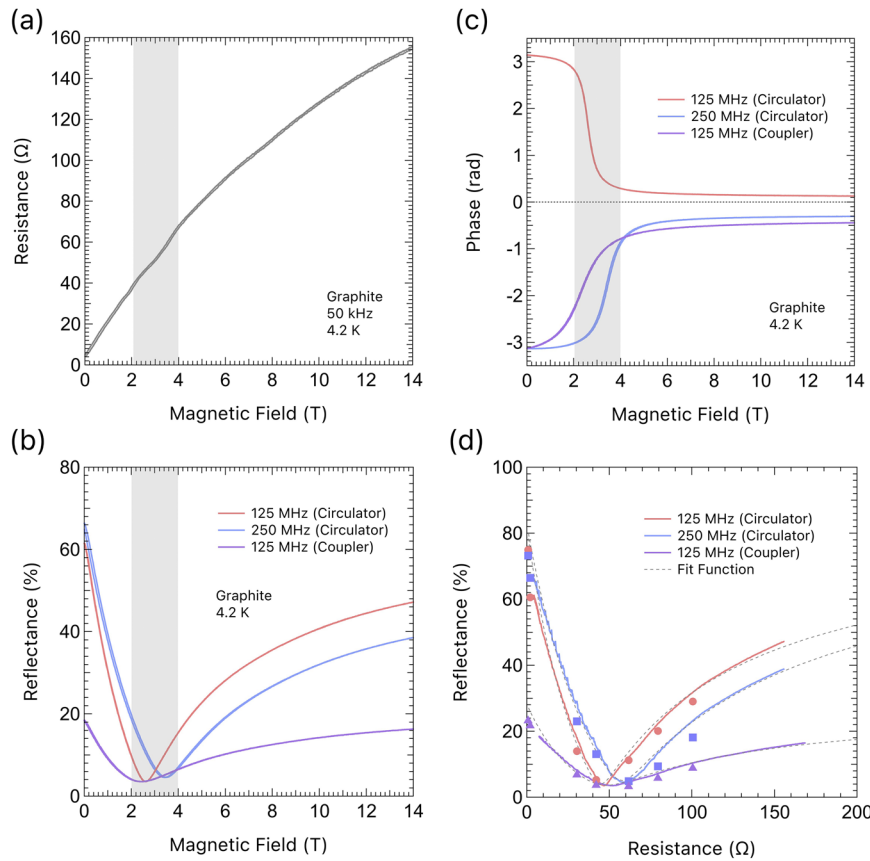


FIG. 2. (a) Two-terminal resistance of FIB-processed graphite, measured by the AC technique in the non-destructive pulsed magnetic field; (b) reflectance and (c) phase shift, obtained by RF measurements. Reflectance shows the ratio of the amplitude of the reflected wave to that of the reference wave, and phase shift represents the difference in the phase of those waves. A constant background caused by the phase rotation during propagation in the coaxial cable has been subtracted from the measured phase. The gray hatched area shows the magnetic field region of 2–4 T, where the magnetoresistance of graphite reaches around 50 Ω , which is the characteristic impedance of the transmission line. (d) Reflectance vs resistance plot. The red solid line shows the data at 125 MHz, obtained with the circulator. The blue solid line shows the data at 250 MHz, obtained with the circulator. The purple solid line shows the data obtained at 125 MHz with the directional coupler. The circles, squares, and triangles represent the data obtained from the chip resistors. The gray dashed line shows the fit curve obtained by Eq. (6).

resistance is nearly zero and the system can be regarded as a short circuit, θ_S is close to $\pm\pi$, which is equivalent to the fixed-end reflection. In the higher field, where the sample resistance reaches several hundreds of ohm, which can be regarded as the free-end reflection, θ_S approaches zero. At around fields where $R \sim Z_0$ (impedance matched), θ_S changes drastically. The qualitative difference in the sign of θ_S is attributed to the variation in the susceptance of the circuit.

In Fig. 2(d), the solid curves represent the relationship between the reflectance and the resistance of graphite, derived from Figs. 2(a) and 2(b). The filled circles show the data obtained from chip resistors. The positions of the dips in the curves provide information on Z_0 of the measurement system at each setup. The dashed lines show the fit function of the obtained Γ vs R curves. The fitting procedure is performed as follows: As in Eq. (1), Γ_S is the absolute value of ρ , which can be transformed as

$$\Gamma_S = |\rho| = \left| \frac{1 - y}{1 + y} \right| = \left| \frac{1 - g - ib}{1 + g + ib} \right| = \left| \frac{R - Z_0 - iRb}{R + Z_0 + iRb} \right|. \quad (5)$$

Therefore, the observed Γ vs R curves can be fitted by using the following function

$$\Gamma = A\Gamma_S = A\sqrt{\frac{(R - Z_0)^2 + (Rb)^2}{(R + Z_0)^2 + (Rb)^2}}, \quad (6)$$

where A is a parameter that relates to several factors, such as the attenuation in the transmission line and coupling constant between the ports of the splitter/circulator/directional coupler. Table I presents the fit parameters obtained from the above fits.

TABLE I. Fitting parameters of Γ vs R data, obtained by using Eq. (6). A is the maximum reflectance, Z_0 is the characteristic impedance, and $|b|$ is the absolute value of susceptance.

Setup	A	Z_0 (Ω)	$ b $
125 MHz (circulator)	0.79	43.8	0.11
250 MHz (circulator)	0.83	58.2	0.12
125 MHz (directional coupler)	0.28	49.9	0.26

In Fig. 3, the reflectance of the sample at $\Gamma_S = \Gamma/A$ and phase θ_S are plotted as the polar coordinates, which is identical to plotting the complex reflection coefficient ρ on the uv -plane. An admittance chart is overlaid on the plot, which provides a graphical representation of ρ in terms of conductance and susceptance. The observed value of the phase shift θ contains the influence of the extrinsic phase rotations within the transmission line and electric parts of the present setup. Since the degree of the extrinsic phase shift depends on the length of the cable and measurement frequency, a constant background is subtracted from θ to obtain θ_S , which is equivalent to rotating the plot around the origin in Fig. 3 [See Eq. (1)]. In the present case, the conductance of the graphite sample changes as a function of the field, while the capacitance of the graphite sample should keep a constant value. Therefore, θ_S is determined as the trace of ρ , aligned on the constant susceptance circle of the admittance chart. Regardless of the measurement frequencies, ρ changes from the left side to the right side of the admittance chart with increasing magnetic fields, which represents a decrease in conductance,

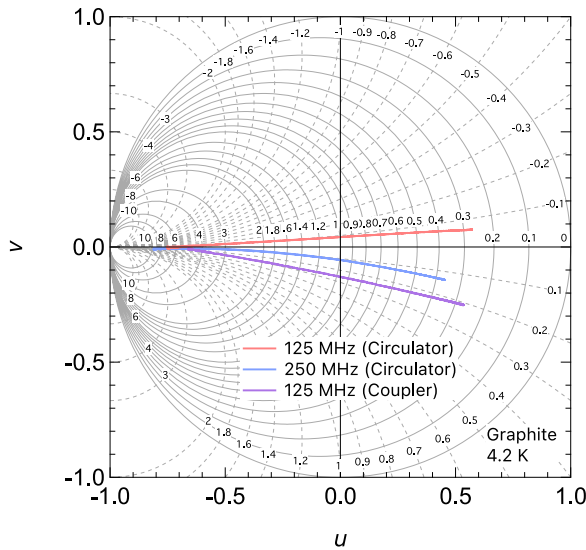


FIG. 3. Γ_S and θ_S are plotted on the uv -plane, using polar coordinates along with an admittance chart. The red line shows the data at 125 MHz using a circulator, while the blue line represents the data at 250 MHz. The purple line corresponds to the data at 125 MHz using directional coupler. Solid and dashed gray lines show the constant conductance circle and the constant susceptance circle of the admittance chart, respectively. The numbers on the circles represent the value of conductance and susceptance of each line, which are normalized by the fitted values of Z_0 .

or equivalently, an increase in resistance of the graphite sample. The values of the constant susceptance circles, along which ρ is aligned, depend on the frequency and the measurement setup. This might be attributed to the differences in the parasitic inductance or capacitance of the measurement circuit.

Figures 4(a) and 4(b) shows the field dependence of resistance and susceptance of graphite, respectively, which are calculated from the ρ curves plotted in Fig. 3. By applying Eqs. (3) and (4), they are converted into normalized conductance and susceptance, respectively. The resistance is obtained by $R = Z_0/g$, and the susceptance B is calculated by $B = b/Z_0$. The calculated resistance curves exhibit good agreement with the two-terminal magnetoresistance measured at the low frequency of 50 kHz. By ignoring the imaginary part of ρ and substituting it in Eq. (2) as in the previous reports,^{11–13,15} the resistance curves were also evaluated, as seen in

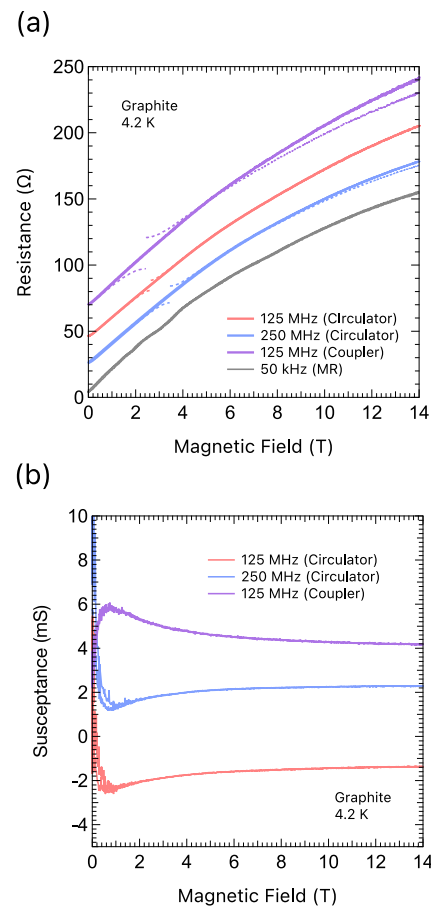


FIG. 4. (a) Magnetoresistance of FIB-processed graphite obtained from RF impedance and two-terminal AC resistance measurements. The purple solid line shows the data at 125 MHz, obtained with the directional coupler. The red solid line shows the data at 125 MHz, obtained with the circulator. The blue solid line shows the data at 250 MHz, obtained with the circulator. The black line represents the AC magnetoresistance at 50 kHz. Dashed lines represent the magnetoresistance, calculated using the conventional method. Each line is offset by 20 Ω . (b) Magnetic-field dependence of susceptance, obtained from RF impedance measurements.

the dashed curves in Fig. 4(a). When comparing the magnetoresistance curves obtained by Eqs. (3) and (4) (solid curves) with those obtained by Eq. (2), it is clear that the magnetoresistance calculated by Eq. (2) exhibits discontinuities when the magnetoresistance crosses the value of characteristic impedance. We found that the field dependence of susceptance remains nearly constant above 2 T, while the magnetoresistance shows an extremely large increase from 5 (Ω) to 150 Ω (14 T). The fluctuations of 6 mS observed near zero magnetic field are due to the poor sensitivity on the left side of the admittance chart, where the constant susceptance circles are densely gathered.

B. Measurements with STC

RF impedance measurements at 140 MHz were performed in STC, and standard two-terminal resistance measurements at 50 kHz were conducted in the non-destructive magnet. The YBCO sample was immersed in liquid nitrogen. In the non-destructive magnet, magnetic fields up to 57 T were generated, and the magnetoresistance was measured in helium gas cooled by liquid nitrogen.

In Fig. 5(a), the converted magnetoresistance obtained from RF impedance measurements in STC at 77.4 K is presented

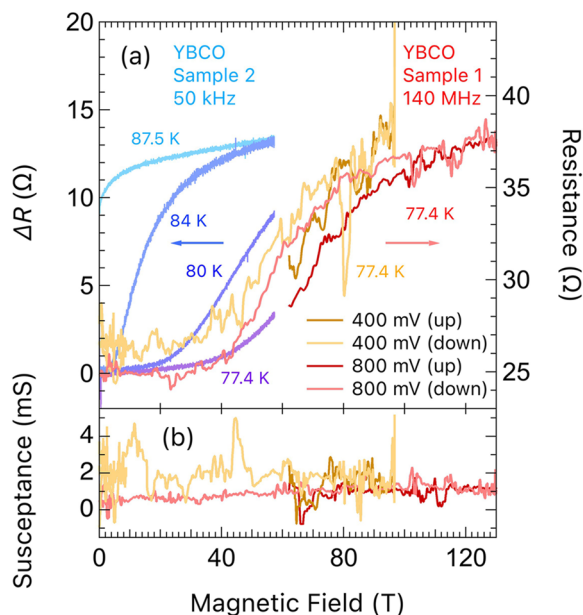


FIG. 5. (a) Magnetic field dependence of resistance of YBCO superconducting film. Yellow and red lines show the calculated resistance of sample 1 obtained from 140 MHz RF impedance measurements at 77.4 K with STC (right axis). The dark and light yellow lines represent the data obtained with the source amplitude of 400 mV in the increasing and decreasing magnetic field, respectively. The dark and light red lines represent the data obtained with the source amplitude of 800 mV in the increasing and decreasing field, respectively. Cyan, blue, cobalt, and purple lines show the change of magnetoresistance ΔR of sample 2, obtained from 50 kHz standard two-terminal measurements with the non-destructive magnet at 87.5, 84, 80, and 77.4 K, respectively (left axis); (b) field dependence of susceptance obtained from RF measurements of sample 1 with STC.

(sample 1, right axis), along with the magnetoresistance change ΔR of YBCO obtained from two-terminal measurements in the non-destructive magnet at several temperatures (sample 2, left axis). For the STC data, the signal within $\sim 1 \mu\text{s}$ after the pulse generation was excluded from the analysis due to the noise accompanied by the field generation. The RF data were analyzed using an admittance chart and converted into resistance and susceptance, where the attenuation coefficient A and characteristic impedance Z_0 were set to be 0.8 and 44 Ω , respectively. Two STC experiments were performed with maximum magnetic fields of 100 and 130 T, and RF waves with a frequency of 140 MHz and peak-to-peak amplitudes of 400 and 800 mV were used, respectively. The data obtained with the amplitude of 800 mV shows a higher S/N ratio. To further improve the S/N ratio, increasing the excitation voltage or applying a narrower bandpass filter can be effective. In addition, the elimination of the electromagnetic noise caused by the field generation might be achieved by developing electromagnetic shielding against the STC system.²³ The contribution of the contact resistance was not subtracted. The slight difference in the zero-field resistance in each experiment is probably due to the change in the contact resistance. For the data obtained with the non-destructive magnet, the contribution of the contact resistance was subtracted to estimate ΔR , because the contact resistance depended on temperature. In the experiments in STC, the middle points of the superconducting to the metal transition are located at ~ 65 T. These magnetoresistance data obtained by the RF impedance technique agree with the data taken in the non-destructive magnet at 77.4 K, although there is a slight hysteresis in the data taken with STC. One possibility is that the hysteresis is due to the intrinsic character of the YBCO superconductor.²⁴ Another possibility is the eddy current heating, which occurs in metallic parts of the probe or a metallic sample itself, namely, wires, electrodes, and the YBCO sample. The possible temperature increase caused by the eddy current is estimated to be less than 3 K, considering the magnetoresistance data taken with the non-destructive magnet. We note that our system is expected to be operational at lower temperature. In the previous studies using FPCs,^{10,14,15} the effect of eddy currents was almost negligible even at liquid helium temperatures. Figure 5(b) illustrates the field dependence of susceptance obtained with STC. The susceptance remains nearly constant throughout the measurements. Since the YBCO film is a metallic material, no change in the capacitance component is expected. This confirms that the present analysis successfully corrects the phase backgrounds.

IV. SUMMARY

We applied the RF impedance technique to perform magnetoresistance measurements in ultrahigh magnetic fields above 100 T. The use of a circulator instead of a directional coupler enhanced the separation of reflected waves. Replacing twisted pairs of copper wires with FPCs and semi-rigid coaxial cables reduced the voltage induced by the pulsed field and improved impedance-matching. Additionally, by treating the reflection coefficient as a complex number and utilizing an admittance chart, we achieved the separation of the magnetoresistance and the magnetosusceptance. These advancements provide more precise and comprehensive insights into the electrical properties of materials under magnetic fields.

ACKNOWLEDGMENTS

The authors are grateful to S. Peng, Y. H. Matsuda, and T. Osada. The work at Tokyo Institute of Technology was supported by J. Yamaura and H. Hosono through the Elements Strategy Initiative to Form Core Research Center (Grant No. JPMXP0112101001). This work was partly supported by a JSPS KAKENHI Grant Nos. 22H00104 and 20K14403, the New Energy and Industrial Technology Development Organization (NEDO) Grant No. JPNP20004, and the MEXT Elements Strategy Initiative to Form Core Research Center (Grant No. JPMXP0112101001). The National High Magnetic Field Laboratory is supported by the National Science Foundation through Grant No. NSF/DMR-2128556, and the State of Florida.

AUTHOR DECLARATIONS

Conflict of Interest

The authors have no conflicts to disclose.

Author Contributions

T. Shitaokoshi: Data curation (equal); Formal analysis (lead); Investigation (equal); Writing – original draft (lead). **S. Kawachi:** Data curation (equal); Formal analysis (equal); Investigation (lead); Resources (supporting); Writing – review & editing (equal). **T. Nomura:** Data curation (equal); Formal analysis (equal); Investigation (equal); Resources (supporting); Writing – review & editing (equal). **F. F. Balakirev:** Conceptualization (equal); Investigation (supporting); Methodology (supporting); Resources (supporting); Writing – review & editing (equal). **Y. Kohama:** Conceptualization (equal); Investigation (equal); Project administration (lead); Resources (lead); Supervision (lead); Writing – original draft (supporting); Writing – review & editing (equal).

DATA AVAILABILITY

The data that support the findings of this study are available from the corresponding author upon reasonable request.

REFERENCES

- ¹F. Herlach and R. McBroom, “Megagauss fields in single turn coils,” *J. Phys. E: Sci. Instrum.* **6**, 652 (1973).
- ²T. Takamasu, H. Nakagawa, and N. Miura, “Transport measurements in short pulsed fields up to 100 T,” *Physica B* **216**, 362–365 (1996) [Proceedings of the International Workshop on Advances in High Magnetic Fields].
- ³H. Nakagawa, T. Takamasu, N. Miura, and Y. Enomoto, “DC and AC magneto-resistance measurement technique for $\text{YBa}_2\text{Cu}_3\text{O}_{7-\delta}$ thin films in megagauss fields,” *Physica B* **246–247**, 429–432 (1998).
- ⁴N. Miura, H. Nakagawa, T. Sekitani, M. Naito, H. Sato, and Y. Enomoto, “High-magnetic-field study of high- T_c cuprates,” *Physica B* **319**, 310–320 (2002).
- ⁵Y. Shimamoto, N. Miura, and H. Nojiri, “Magnetic-field-induced electronic phase transitions in semimetals in high magnetic fields,” *J. Phys.: Condens. Matter* **10**, 11289 (1998).
- ⁶T. Sakakibara, T. Goto, and N. Miura, “Contactless transport measurement of metals in pulsed high magnetic fields,” *Rev. Sci. Instrum.* **60**, 444–449 (1989).
- ⁷T. Sekitani, Y. Matsuda, S. Ikeda, K. Uchida, F. Herlach, N. Miura, K. Nakao, T. Izumi, S. Tajima, M. Murakami, S. Hoshi, T. Koyama, and Y. Shiohara, “Transport measurements of high- T_c superconductors at megagauss magnetic fields by means of a radio frequency transmission technique,” *Physica C* **392–396**, 116–122 (2003) [Proceedings of the 15th International Symposium on Superconductivity (ISS, 2002): Advances in Superconductivity XV. Part I].
- ⁸T. Sekitani, Y. H. Matsuda, and N. Miura, “Measurement of the upper critical field of optimally-doped $\text{YBa}_2\text{Cu}_3\text{O}_{7-\delta}$ in megagauss magnetic fields,” *New J. Phys.* **9**, 47 (2007).
- ⁹D. Nakamura, M. M. Altarawneh, and S. Takeyama, “Radio frequency self-resonant coil for contactless AC-conductivity in 100 T class ultra-strong pulse magnetic fields,” *Meas. Sci. Technol.* **29**, 035901 (2018).
- ¹⁰Y. Kohama, F. Nabeshima, A. Maeda, A. Ikeda, and Y. H. Matsuda, “Direct measurement of resistivity in destructive pulsed magnetic fields,” *Rev. Sci. Instrum.* **91**, 033901 (2020).
- ¹¹M. Saito, T. Inokuchi, E. Ohmichi, K. Uchida, and T. Osada, “Transport measurement for low-dimensional conductors under ultra-high magnetic fields beyond 100 T,” *Synth. Met.* **133–134**, 133–135 (2003) [Proceedings of the Yamada Conference LVI. The Fourth International Symposium on Crystalline Organic Metals, Superconductors and Ferromagnets (ISCOM 2001)].
- ¹²T. Inokuchi, T. Osada, S. Ikeda, K. Uchida, M. Kuraguchi, A. Ogasawara, E. Ohmichi, and N. Miura, “Transport measurement of two-dimensional electron system under ultra-high magnetic fields,” *Physica E* **22**, 381–384 (2004) [15th International Conference on Electronic Properties of Two-Dimensional Systems (EP2DS-15)].
- ¹³H. Imamura, K. Uchida, E. Ohmichi, and T. Osada, “Magnetotransport measurements of low dimensional conductors under pulsed ultra-high magnetic fields,” *J. Phys.: Conf. Ser.* **51**, 303 (2006).
- ¹⁴K. Hanzawa, J. Matsumoto, S. Iimura, Y. Kohama, H. Hiramatsu, and H. Hosono, “High upper critical field (120 T) with small anisotropy of highly hydrogen-substituted SmFeAsO epitaxial film,” *Phys. Rev. Mater.* **6**, L111801 (2022).
- ¹⁵S. Kawachi, J. Yamaura, Y. Kuramoto, S. Iimura, T. Nomura, Y. Kohama, T. Sasaki, M. Tokunaga, Y. Murakami, and H. Hosono, “Distinctive doping dependence of upper critical field in iron-based superconductor $\text{LaFeAsO}_{1-x}\text{H}_x$,” *Phys. Rev. B* **108**, L100503 (2023).
- ¹⁶D. Pavlidis and H. Hartnagel, “The design and performance of three-line microstrip couplers,” *IEEE Trans. Microwave Theory Tech.* **24**, 631–640 (1976).
- ¹⁷V. Tripathi, “On the analysis of symmetrical three-line microstrip circuits,” *IEEE Trans. Microwave Theory Tech.* **25**, 726–729 (1977).
- ¹⁸P. Xie, P. Gu, and J. J. Beaudoin, “Contact capacitance effect in measurement of a.c. impedance spectra for hydrating cement systems,” *J. Mater. Sci.* **31**, 144–149 (1996).
- ¹⁹P. K. Basu and H. Dhasmana, “Introduction to Smith chart,” in *Electromagnetic Theory* (Springer International Publishing, Cham, 2023), pp. 165–181.
- ²⁰T. Mizuhashi, “Theory of four-terminal impedance transformation circuit and matching circuit,” *J. Inst. Electric. Commun. Eng. Jpn.* **20**, 1053 (1937).
- ²¹P. H. Smith, “Transmission line calculator,” *Electronics* **12**, 29–31 (1939).
- ²²P. H. Smith, *An Improved Transmission Line Calculator* (Livermore and Knight Company, 1941).
- ²³S. Peng and Y. H. Matsuda, private communication (2023).
- ²⁴R. Marcon, R. Fastampa, M. Giura, and E. Silva, “Vortex-motion dissipation in high- T_c superconductors at microwave frequencies,” *Phys. Rev. B* **43**, 2940–2945 (1991).